Computational Particle Mechanics (2019) 6:515–527
https://doi.org/10.1007/s40571-019-00230-7

Simulations for the explosion in a water-filled tube including cavitation using the SPH method

Jian-Yu Chen[1] · Chong Peng[2,3] · Fue-Sang Lien[1,4] · Eugene Yee[1] · Xiao-Hua Zhao[5]

Received: 12 November 2018 / Revised: 26 January 2019 / Accepted: 19 February 2019 / Published online: 1 March 2019

Abstract
The damage to a structure due to an underwater explosion, which must necessarily include the phenomenon of cavitation, is a difficult problem to simulate. In this paper, the smoothed particle hydrodynamics (SPH) method is used to address the simulation of a fully explicit three-dimensional (3D) underwater explosion in a rigid or deformable cylinder, incorporating properly the physical phenomenon of cavitation. To this purpose, a general 3D SPH code has been implemented using the Open-MP programming interface. The various components of the code have been validated using four test cases, namely the Sjögreen test case for validation of the Riemann solver, the 1D cavitating flow in an open tube test case for validation of the cavitation model, the 1D pentaerythritol tetranitrate detonation test case for validation of the Jones–Wilkins–Lee model and a 3D high-velocity impact test case for validation of the elastic–perfectly plastic constitutive model. Following this validation, a 3D explosion within a water-filled rigid cylinder and a water-filled deformable aluminum tube are simulated with the general SPH code. The results of these simulations are compared against some available experimental data and some numerical simulations obtained using an alternative approach. These comparisons are generally in good agreement with both the experimental and numerical data, demonstrating that the SPH method can be used to simulate general 3D underwater explosion problems.

Keywords Cavitation · Cylindrical structure · Open-MP · Smoothed particle hydrodynamics · Underwater explosion

1 Introduction

An important research endeavor in naval weapon systems design is the prediction of underwater explosions and their effects on ships and submarines. Approaches for the prediction of an underwater explosion and concomitant damage to structures range from experimentation to simulation. However, experiments (trials) that investigate the effects of shock waves on ships have limited utility owing to their prohibitive cost and difficulties in the measurement of the phenomena involved. In view of this, numerical simulation is an alternative method that can be used for the investigation of the spectrum of complex physical processes involved in an underwater explosion.

Conventional simulation methods such as the finite difference method (FDM), finite volume method (FVM) and the finite element method (FEM) have been widely applied in

✉ Chong Peng
chong.peng@essteyr.com

Jian-Yu Chen
j492chen@uwaterloo.ca

Fue-Sang Lien
fslien@uwaterloo.ca

Eugene Yee
eyee0309@gmail.com

Xiao-Hua Zhao
zhaoxh@whu.edu.cn

[1] Department of Mechanical and Mechatronics Engineering, University of Waterloo, 200 University Avenue West, Waterloo, ON N2L 3G1, Canada

[2] ESS Engineering Software Steyr GmbH, Berggasse 35, 4400 Steyr, Austria

[3] Institut für Geotechnik, Universität für Bodenkultur, Feistmantelstrasse 4, 1180 Vienna, Austria

[4] Key Laboratory of Metallurgical Equipment and Control Technology of Ministry of Education, Wuhan University of Science and Technology, Wuhan 430081, Hubei, China

[5] State Key Laboratory of Water Resources and Hydropower Engineering Science, Wuhan University, Wuhan 430072, China

engineering and science. However, these grid-based numerical methods have a number of deficiencies in their ability to address explosion simulations. For example, the meshing and remeshing of the solution domain for explosion simulations are time-consuming. Moreover, extreme distortions of the mesh that may result in this remeshing can provoke numerical instabilities that can culminate in a program crash. In consequence, traditional numerical methods for explosion simulation are frequently augmented with various other strategies in order to resolve various numerical difficulties associated with the simulation. As an example of this approach [1], a boundary element method (BEM) such as the doubly asymptotic approximation (DAA) is used to simulate the movement of the water due to an explosion, whereas a FEM is used to model the effects of the explosion on the structure. Other strategies involve the combination of a Lagrangian and an Eulerian grid framework in which a Lagrangian mesh is used to track the material interface, while an Eulerian mesh is used to model the large deformations that characterize an underwater explosion [2,3]. Zhang et al. [4] coupled a Runge–Kutta discontinuous Galerkin (RKDG) method with a FEM in order to investigate the cavitation problem induced in the near field of an underwater explosion [4].

Recently, there has been a growing interest in the application of particle methods for explosion simulation, owing to the fact that these methods can track the changing material interface easily and, hence, are more applicable to addressing detonation problems involving large deformations. In this paper, a gridless methodology known as smoothed particle hydrodynamics (SPH) [5,6] is used to address underwater explosion problems. Although this approach was originally applied for the simulation of astrophysical phenomena, it has been used in various computational fluid dynamics (CFD) problems, especially those that involve multi-phase processes owing to the fact that the rates of change of physical variables in the governing equations can be obtained readily through particle–particle interactions.

In some seminal work, Swegel [7] investigated the feasibility of using the SPH method to simulate an underwater explosion and demonstrated that the SPH method can capture the shock wave and treat the large deformations that characterize detonation phenomenology well. Liu et al. [8] simulated air and underwater explosions using the SPH method. Fan and Li [9,10] investigated three-dimensional (3D) landmine detonation using the SPH methodology in conjunction with Open-MP. Zhao et al. [11] simulated underwater explosions and their effects on steel and reinforced concrete slabs using the SPH method. Zhang et al. [12] investigated bubble pulsing, jet formation and shock wave propagation in an underwater explosion using a combination of the SPH method and BEM.

Currently, SPH simulations of an underwater explosion are mostly limited to two-dimensional (2D) models. Although some 3D underwater explosion problems such as an axial symmetrical column charge detonation can be converted to a 2D problem and simulated using an axisymmetric SPH method, it is still difficult to address general 3D explosion problems using the SPH method, owing to the fact that these problems are extremely compute-intensive [12]. In view of this situation, our research group has developed a general 3D in-house SPH code [13,14] based on a strategy described by Liu and Liu [15]. The Open-MP programming interface has been utilized in this code in order to reduce the computational time (viz. to improve significantly the computational efficiency of a simulation involving a large number of particles required for 3D underwater explosion simulations). To this purpose, we have applied this code to the simulation of an underwater explosion within a rigid cylinder and a deformable aluminum tube, including the phenomenon of cavitation for the first time using the SPH method. Furthermore, the 3D underwater explosion in a tube is simulated directly as a full 3D problem, rather than reducing it to a 2D problem by using a 2D cylindrical coordinate system as has been done in previous investigations [16,17].

The paper is organized as follows. The fundamental principles underpinning the SPH method is presented in Sect. 2. The test cases used for validation of our SPH code for explosion simulations, as well as the validation of the various components of our code, are described in Sect. 3. The simulation of a 3D underwater explosion within a rigid cylinder and a deformable aluminum tube is presented in Sect. 4. Section 5 summarizes the key conclusions of this work.

2 Fundamentals of the SPH method

2.1 Function approximation in SPH

In a conventional SPH method, an arbitrary function $f(\boldsymbol{x})$ is approximated (estimated) by convolving the function with a kernel function $W(\boldsymbol{x}, h)$ [15],

$$\langle f(\boldsymbol{x})\rangle = \int_{\Omega} f(\boldsymbol{x}')W(\boldsymbol{x}-\boldsymbol{x}', h)\mathrm{d}\boldsymbol{x}' \,, \tag{1}$$

where h is the smoothing length (kernel radius). The particle approximation for $f(\boldsymbol{x})$ can be obtained from the discretization of Eq. 1 as follows:

$$\langle f(\boldsymbol{x}_i)\rangle = \sum_{j=1}^{N} f(\boldsymbol{x}_j)W_{ij}\frac{m_j}{\rho_j} \,, \tag{2}$$

where $W_{ij} \equiv W(\boldsymbol{x_i}-\boldsymbol{x_j}, h)$, m_j and ρ_j are the mass and density for particle j, respectively, and N is the total number

of particles used in the simulation. There are many choices for the kernel function $W(\boldsymbol{x}, h)$. In this paper, we will use the Gaussian kernel function given by

$$W(R,h) = \begin{cases} \alpha_d e^{-R^2}, & 0 \le R \le 3\,; \\ 0, & R > 3\,. \end{cases} \tag{3}$$

Here, R is the normalized distance from particle i to particle j defined as $R \equiv r/h = |\boldsymbol{x_i} - \boldsymbol{x_j}|/h$ and α_d is a normalization factor given by $1/(\pi h^2)$ in two dimensions and $1/(\pi^{\frac{3}{2}} h^3)$ in three dimensions.

2.2 Discretized equations for the Navier–Stokes (N–S) equation

The stress tensor $\sigma^{\alpha\beta}$ is defined in terms of a symmetrical deviatoric stress tensor $S^{\alpha\beta}$ and an isotropic tensor $p\delta^{\alpha\beta}$ as

$$\sigma^{\alpha\beta} = -p\delta^{\alpha\beta} + S^{\alpha\beta}\,. \tag{4}$$

The Navier–Stokes equation can be discretized in the SPH methodology as follows [15]:

$$\begin{cases} \frac{\mathrm{d}\rho_i}{\mathrm{d}t} = \sum_{j=1}^{N} m_j v_{ij}^{\alpha} \frac{\partial W_{ij}}{\partial x_i^{\alpha}}\,, & \text{(a)} \\ \frac{\mathrm{d}v_i^{\alpha}}{\mathrm{d}t} = \sum_{j=1}^{N} m_j \left(\frac{\sigma_i^{\alpha\beta} + \sigma_j^{\alpha\beta}}{\rho_i \rho_j} + \Pi_{ij}\delta^{\alpha\beta} \right) \frac{\partial W_{ij}}{\partial x_i^{\beta}}\,, & \text{(b)} \\ \frac{\mathrm{d}e_i}{\mathrm{d}t} = \frac{1}{2}\sum_{j=1}^{N} m_j \left(\frac{p_i + p_j}{\rho_i \rho_j} + \Pi_{ij} \right) v_{ij}^{\beta} \frac{\partial W_{ij}}{\partial x_i^{\beta}} \\ \qquad + \frac{1}{2\rho_i} S_i^{\alpha\beta} \varepsilon_i^{\alpha\beta} + \Delta W_{\mathrm{p}}^{(n)}\,, & \text{(c)} \\ p_i = p(\rho_i, e_i)\,, & \text{(d)} \end{cases} \tag{5}$$

where ρ_i, v_i, e_i, p_i and m_i are density, velocity, internal energy, pressure and mass of particle i, respectively; $\mathrm{d}(\,\cdot\,)/\mathrm{d}t$ is the time derivative; $v_{ij}^{\alpha} \equiv v_i^{\alpha} - v_j^{\alpha}$; $\varepsilon_i^{\alpha\beta}$ is the strain rate component of particle i; Π_{ij} is the Monaghan artificial viscosity which is described in Sect. 2.3; $\Delta W_{\mathrm{p}}^{(n)}$ is the incremental plastic work at the nth time step which is presented in Sect. 2.4; and the equation of state (EOS) [Eq. (5d)] is given in Sect. 2.5.

2.3 Artificial viscosity

The Monaghan-type artificial viscosity [18] is incorporated into SPH in order to smooth potential unphysical oscillations, to prevent unphysical particle–particle penetration and to stabilize the numerical solutions. This artificial viscosity assumes the following form:

$$\Pi_{ij} = \begin{cases} \frac{-\alpha c_{ij}\phi_{ij} + \beta\phi_{ij}^2}{\rho_{ij}}\,, & \boldsymbol{v_{ij}} \cdot \boldsymbol{x_{ij}} < 0\,; \\ 0\,, & \boldsymbol{v_{ij}} \cdot \boldsymbol{x_{ij}} \ge 0\,. \end{cases} \tag{6}$$

Here, $\phi_{ij} = \frac{h_{ij}\boldsymbol{v_{ij}}\cdot\boldsymbol{x_{ij}}}{|\boldsymbol{x_{ij}}|^2 + (\varphi)^2}$, $c_{ij} = \frac{1}{2}(c_i + c_j)$, $\rho_{ij} = \frac{1}{2}(\rho_i + \rho_j)$, $h_{ij} = \frac{1}{2}(h_i + h_j)$, $\boldsymbol{v_{ij}} = \boldsymbol{v_i} - \boldsymbol{v_j}$, and $\boldsymbol{x_{ij}} = \boldsymbol{x_i} - \boldsymbol{x_j}$, where c_i is the speed of sound associated with particle i; α and β are constant coefficients that are set to have values of 1.0 and 10.0, respectively; and $\varphi = 0.1 h_{ij}$ is applied in order to prevent the unphysical overlapping of two particles.

2.4 Elastic–perfectly plastic constitutive model for solids

The elastic–perfectly plastic constitutive relation is used for the solid impact between two particles and is formulated as follows. The Jaumann rate of stress $\dot{S}_J^{\alpha\beta}$ is widely used for this purpose [19] and is related to the stress tensor as follows:

$$\dot{S}^{\alpha\beta} = \dot{S}_J^{\alpha\beta} + S^{\alpha\gamma}\dot{w}^{\beta\gamma} + S^{\gamma\beta}\dot{w}^{\alpha\gamma}\,. \tag{7}$$

For a material in the elastic range,

$$\dot{S}_J^{\alpha\beta} = 2G\left(\dot{\varepsilon}^{\alpha\beta} - \frac{1}{3}\delta^{\alpha\beta}\dot{\varepsilon}^{\gamma\gamma}\right)\,, \tag{8}$$

where G is the shear modulus. With the Jaumann rate of stress, the evolution of the trial elastic stress can be obtained from Eqs. (7) and (8) as

$$\begin{aligned} S_{\mathrm{e}}^{\alpha\beta} &= \Delta t\left(2G\left(\dot{\varepsilon}^{\alpha\beta} - \frac{1}{3}\delta^{\alpha\beta}\dot{\varepsilon}^{\gamma\gamma}\right) + S^{\alpha\gamma}\dot{w}^{\beta\gamma} \right. \\ &\quad \left. + S^{\gamma\beta}\dot{w}^{\alpha\gamma}\right) + S_{(n)}^{\alpha\beta}\,, \end{aligned} \tag{9}$$

where $S_{(n)}^{\alpha\beta}$ is the deviatoric stress component at the nth time step. The strain rate and rotation rate tensors are defined as

$$\dot{\varepsilon}^{\alpha\beta} = \frac{1}{2}\left(\frac{\partial v^{\alpha}}{\partial x^{\beta}} + \frac{\partial v^{\beta}}{\partial x^{\alpha}}\right) \tag{10}$$

and

$$\dot{w}^{\alpha\beta} = \frac{1}{2}\left(\frac{\partial v^{\alpha}}{\partial x^{\beta}} - \frac{\partial v^{\beta}}{\partial x^{\alpha}}\right)\,. \tag{11}$$

The particle approximations for the strain rate and spin rate components can be obtained from

$$\dot{\varepsilon}_i^{\alpha\beta} = \frac{1}{2}\sum_{j=1}^{N}\frac{m_j}{\rho_j}\left(v_{ji}^{\alpha}\frac{\partial W_{ij}}{\partial x_i^{\beta}} + v_{ji}^{\beta}\frac{\partial W_{ij}}{\partial x_i^{\alpha}}\right) \tag{12}$$

and

$$\dot{w}_i^{\alpha\beta} = \frac{1}{2}\sum_{j=1}^{N}\frac{m_j}{\rho_j}\left(v_{ji}^{\alpha}\frac{\partial W_{ij}}{\partial x_i^{\beta}} - v_{ji}^{\beta}\frac{\partial W_{ij}}{\partial x_i^{\alpha}}\right), \tag{13}$$

where $v_{ji}^{\alpha} = v_j^{\alpha} - v_i^{\alpha}$. The second invariant J_2 of the deviatoric part of the elastic trial stress $S_{\mathrm{e}}^{\alpha\beta}$ is

$$J_2 = \frac{1}{2}S_{\mathrm{e}}^{\alpha\beta}S_{\mathrm{e}}^{\alpha\beta}\ . \tag{14}$$

The plastic regime is determined by von Mises criterion when the second invariant J_2 is greater than one-third of the square of the yield stress σ_{Y}. In this case, the components of the deviatoric stress tensor are brought back to the yield surface in accordance with

$$S^{\alpha\beta} = \begin{cases} S_{\mathrm{e}}^{\alpha\beta}\ , & \text{if } J_2 \le \sigma_{\mathrm{Y}}^2/3\ ; \\ \sqrt{\frac{\sigma_{\mathrm{Y}}^2}{3J_2}}S_{\mathrm{e}}^{\alpha\beta}\ , & \text{if } J_2 > \sigma_{\mathrm{Y}}^2/3\ . \end{cases} \tag{15}$$

The Johnson–Cook model that accounts for thermal softening, high strain rates and strain hardening is used to calculate the plastic yield stress σ_{Y} [20]:

$$\sigma_{\mathrm{Y}} = \left[A + B(\varepsilon_{\mathrm{p}})^n\right]\left[1 + C\ln\left(\frac{\dot{\varepsilon_{\mathrm{p}}}}{\dot{\varepsilon_0}}\right)\right]\left[1 - (T^*)^k\right], \tag{16}$$

where ε_{p} is the equivalent plastic strain, $\dot{\varepsilon_{\mathrm{p}}}$ is the equivalent plastic strain rate and $\dot{\varepsilon_0} = 1\ \mathrm{s}^{-1}$. Furthermore, T^* is the dimensionless temperature which is defined as

$$T^* = \frac{T - T_{\mathrm{room}}}{T_{\mathrm{melt}} - T_{\mathrm{room}}}\ , \tag{17}$$

where T_{room} is the room temperature, T_{melt} is the melting temperature, T is the temperature, and A, B, C, k and n are coefficients that define the material properties.

The incremental plastic work is determined from

$$\Delta W_{\mathrm{p}}^{(n)} = \frac{1}{2}\left(\sigma_{\mathrm{p}}^{(n+1)} + \sigma_{\mathrm{p}}^{(n)}\right)\Delta\varepsilon_{\mathrm{p}}^{(n)}\left(\frac{m}{\rho^{(n+1/2)}}\right)\ , \tag{18}$$

where σ_{p} at the $(n+1)$th time step is calculated from the deviatoric stress tensor $\mathbf{S}_{\mathrm{e}}^{(n+1)}$ as follows:

$$\sigma_{\mathrm{p}}^{(n+1)} = \left(\frac{3}{2}\mathbf{S}_{\mathrm{e}}^{(n+1)} : \mathbf{S}_{\mathrm{e}}^{(n+1)}\right)^{1/2}\ . \tag{19}$$

Finally, the incremental equivalent plastic strain is determined from

$$\Delta\varepsilon_{\mathrm{p}}^{(n)} = \frac{\sigma_{\mathrm{p}}^{(n)} - \sigma_{\mathrm{Y}}}{3G}\ . \tag{20}$$

2.5 The EOS of solids and compressible flow

We use the Mie–Gruneisen equation [21] for the EOS of the solids used in the simulations conducted in this paper. This EOS assumes the following form:

$$p = \left(1 - \frac{1}{2}\Gamma\eta\right)P_H(\rho) + \Gamma\rho E\ , \tag{21}$$

where

$$P_H(\rho) = \begin{cases} a_0\eta + b_0\eta^2 + c_0\eta^3\ , & \eta > 0\ ; \\ a_0\eta\ , & \eta \le 0\ . \end{cases} \tag{22}$$

Here, $\eta = \rho/\rho_0 - 1$ is used to represent the compression; Γ is the Gruneisen parameter; E is the specific internal energy; and the constants a_0, b_0 and c_0 are obtained from

$$\begin{cases} a_0 = \rho_0 C^2\ , \\ b_0 = a_0\left[1 + 2\left(S - 1\right)\right]\ , \\ c_0 = a_0\left[2\left(S - 1\right) + 3\left(S - 1\right)^2\right]\ , \end{cases} \tag{23}$$

where C and S are constant parameters.

The Jones–Wilkins–Lee (JWL) equation is used here to calculate the pressure resulting from a pentaerythritol tetranitrate (PETN) detonation [22]. The JWL equation is given by

$$\begin{aligned} p\ &= A\left(1 - \frac{w\eta_1}{R_1}\right)e^{-\frac{R_1}{\eta_1}} + B\left(1 - \frac{w\eta_1}{R_2}\right)e^{-\frac{R_2}{\eta_1}} \\ &\quad + w\eta_1\rho_0 E\ , \end{aligned} \tag{24}$$

where A, B, R_1, R_2, w are constant parameters; η_1 is the ratio of the detonation products density to the initial density of the explosive; ρ_0 is the initial density; and E is the specific internal energy. A gas bubble in an underwater explosion is assumed to be homogeneous, isentropic and compressible, and the EOS for a gas bubble [16] is determined from

$$p_{\mathrm{g}} = p_0\left(\frac{\rho_{\mathrm{g}}}{\rho_{\mathrm{g}0}}\right)^{\gamma}\ , \tag{25}$$

where p_0 is the initial pressure for the bubble gas; $\rho_{\mathrm{g}0}$ and ρ_{g} are the initial density and the density of the gas, respectively; and the constant γ is taken to have a value of 2 for our underwater explosion simulations. The speed of sound in the gas bubble is determined from

$$a_{\mathrm{g}} = \left(\frac{\mathrm{d}p}{\mathrm{d}\rho}\right)^{\frac{1}{2}} = \left(\frac{p_0\gamma}{\rho_{\mathrm{g}0}}\left(\frac{\rho_{\mathrm{g}}}{\rho_{\mathrm{g}0}}\right)^{\gamma-1}\right)^{\frac{1}{2}}\ . \tag{26}$$

Water is modeled as a compressible fluid and is represented using two different EOSs. One of these EOSs is an

alternative form of the Mie–Gruneisen equation [23] given by

$$p = \begin{cases} \dfrac{\rho_0 C_0^2 \mu \left[1+(1-\frac{\gamma}{2})\mu - \frac{\alpha\mu^2}{2}\right]}{\left[1-(S_1-1)\mu - \frac{S_2\mu^2}{\mu+1} - \frac{S_3\mu^3}{(\mu+1)^2}\right]^2} + (\gamma+\alpha\mu)E\,, & \mu > 0\,; \\ \rho_0 C_0^2 \mu + (\gamma+\alpha\mu)E\,, & \mu \le 0\,, \end{cases} \tag{27}$$

where $\mu = \rho/\rho_0 - 1$, ρ_0 is the initial density, E is the specific internal energy, and S_1, S_2, S_3, γ, α and C_0 are the coefficients of the material. Another EOS for water is Tait's equation where the relation between the density and the pressure is expressed as

$$p_{\mathrm{w}} = B\left(\frac{\rho_{\mathrm{w}}}{\rho_{\mathrm{w0}}}\right)^N - B + A\,, \tag{28}$$

where B and A are constants with values of 3.31×10^8 and 1.0×10^5 Pa, respectively; ρ_{w0} and ρ_{w} are the initial density and the density of water, respectively; and N is a constant with a value of 7.15. The parameter A is set equal to the initial water pressure. The speed of sound in water is given by

$$a_{\mathrm{w}} = \left(\frac{\mathrm{d}p}{\mathrm{d}\rho}\right)^{\frac{1}{2}} = \left(\frac{BN}{\rho_{\mathrm{w0}}}\left(\frac{\rho_{\mathrm{w}}}{\rho_{\mathrm{w0}}}\right)^{N-1}\right)^{\frac{1}{2}}. \tag{29}$$

Both the Mie–Gruneisen EOS and Tait's equation can be used in the simulation of a compressible flow. Tait's equation is the simplest form of EOS for a compressible water flow, and it works well when the pressure is below 20,000 atm. [16]. The Mie–Gruneisen equation of state is suitable for a completely compressible flow, and the variation in the internal energy is properly accounted for in this equation [24].

In the case of an underwater explosion near a structure and a free surface, the cavitation is created just below the free surface or in the vicinity of the structure. The primary difficulties in the simulation of a cavitating flow are in creation and collapse of the cavity. To date, various one-fluid methods have been developed for cavitation simulation in a compressible flow [16,17]. The modified Schmidt cavitation model is one of the most important models in this category and has been used exclusively in underwater explosion simulations [25]. Moreover, this cavitation model is physically stable. As the cavitation flow is assumed to be homogeneous, the density and the pressure of the mixture is governed by the following relationship:

$$\frac{\mathrm{d}p}{\mathrm{d}\rho} = a_{\mathrm{m}}^2\,. \tag{30}$$

The speed of sound a_{m} in the mixture, consisting of vapor and liquid components, is determined from

$$a_{\mathrm{m}} = \left\{[\rho_{\mathrm{l}} + \alpha\cdot(\rho_{\mathrm{v}} - \rho_{\mathrm{l}})]\cdot\left[\frac{\alpha}{\rho_{\mathrm{v}}\cdot a_{\mathrm{v}}^2} + \frac{(1-\alpha)}{\rho_{\mathrm{l}}\cdot a_{\mathrm{l}}^2}\right]\right\}^{-\frac{1}{2}} \tag{31}$$

The pressure of the mixture can be obtained by integrating Eq. (30) after the substitution of a_{m} from Eq. (31). Alternatively, if Tait's EOS is used for pure water, the modified Schmidt cavitation model reduces to the following form:

$$p_{\mathrm{w}} = \begin{cases} B\left(\frac{\rho}{\rho_0}\right)^N - B + A\,, & p \ge p_{\mathrm{sat}}\,; \\ p_{\mathrm{sat}} + p_{\mathrm{gl}}\cdot\ln\left[\frac{\rho_{\mathrm{v}}\cdot a_{\mathrm{v}}^2\cdot(\rho_{\mathrm{l}}+\alpha\cdot(\rho_{\mathrm{v}}-\rho_{\mathrm{l}}))}{\rho_{\mathrm{l}}\cdot\left(\rho_{\mathrm{v}}\cdot a_{\mathrm{v}}^2 - \alpha\cdot\left(\rho_{\mathrm{v}}\cdot a_{\mathrm{v}}^2 - \rho_{\mathrm{l}}\cdot a_{\mathrm{l}}^2\right)\right)}\right], & p_\varepsilon < p < p_{\mathrm{sat}}\,; \\ p_\varepsilon\,, & p \le p_\varepsilon\,, \end{cases} \tag{32}$$

where

$$p_{\mathrm{gl}} = \frac{\rho_{\mathrm{v}}\cdot a_{\mathrm{v}}^2\cdot\rho_{\mathrm{l}}\cdot a_{\mathrm{l}}^2\cdot(\rho_{\mathrm{v}}-\rho_{\mathrm{l}})}{\rho_{\mathrm{v}}^2\cdot a_{\mathrm{v}}^2 - \rho_{\mathrm{l}}^2\cdot a_{\mathrm{l}}^2}\,; \tag{33}$$

a_{v} and a_{l} are the constant speed of sound in the vapor and liquid components (equal to 208 m s^{-1} and 1538 m s^{-1}), respectively; and ρ_{v} and ρ_{l} are constant densities of the vapor and liquid components, respectively. The liquid density is assumed to have a value of $\rho_{\mathrm{l}} = 10^3$ kg m^{-3} and the ratio of vapor to the liquid density is assumed to have a value of $\rho_{\mathrm{v}}/\rho_{\mathrm{l}} = 10^{-5}$. Finally, in Eq. (32), p_ε is a small positive value (about 10^{-5}) and α is the void fraction, which is defined as $\alpha \equiv (\rho - \rho_{\mathrm{l}})/(\rho_{\mathrm{v}} - \rho_{\mathrm{l}})$.

2.6 Boundary conditions

The imposition of boundary conditions is a challenge in the SPH method. Various methodologies have been proposed for the imposition of boundary conditions in SPH simulations [21,26,27]. In this paper, dummy particles are employed to impose the no-slip solid boundary condition at the walls of the rigid cylinder within which the underwater explosion occurs (see Fig. 1). The components of the stress tensor of a real particle i are assigned to all those dummy particles that lie in the support domain $\mathcal{S}$ of this particle; so for, these dummy particles we set $\sigma_d^{\alpha\beta} = \sigma_i^{\alpha\beta}$ for $d \in \mathcal{S}$ [28]. The velocities of the dummy particles v_d are assigned the value of the velocity of the solid boundary v_{w} (viz. $v_d = v_{\mathrm{w}}$).

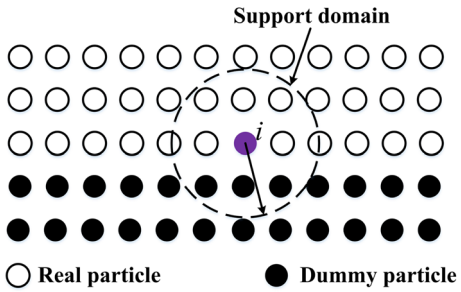

Fig. 1 Depiction of the imposition of the no-slip boundary condition along a solid surface in SPH using dummy particles

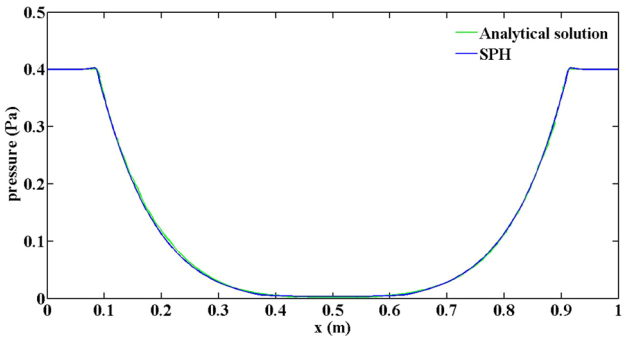

Fig. 2 Comparison of the SPH predictions of the pressure distribution along the shock tube at a time of 0.15 s with an analytical solution

3 Validation of SPH method for explosion simulations

In order to validate our in-house 3D SPH code and physical model, we compare our predictions with some published analytical results and experimental data for the following four test cases, namely for the Sjögreen problem test case, for a 1D cavitating flow in an open tube, for a 1D PETN detonation and for a 3D high-velocity impact test case.

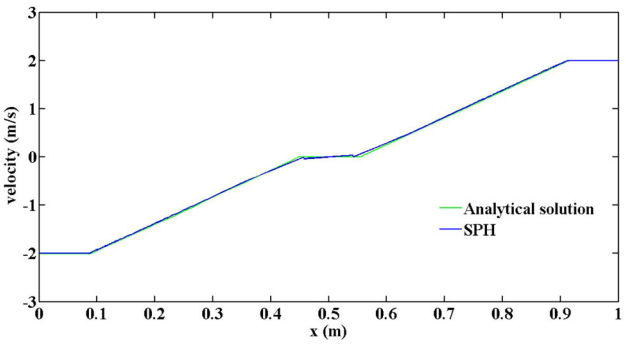

Fig. 3 Comparison of the SPH predictions of the velocity distribution along the shock tube at a time of 0.15 s with an analytical solution

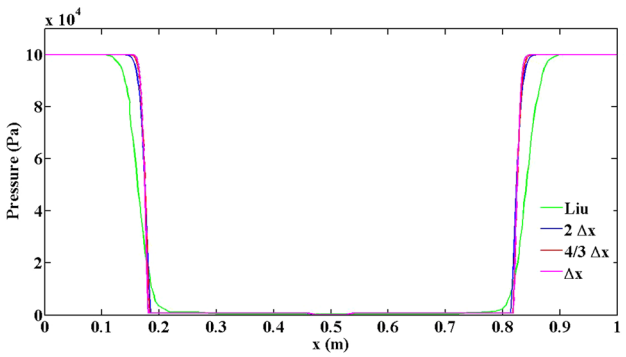

Fig. 4 Comparison of the SPH predictions of the pressure distribution along two water streams at a time of 0.2 ms for three different resolutions with those for a conventional mesh-based method of Liu et al. [16]

3.1 Sjögreen problem

The gas–gas shock tube problem is used here to show that a shock wave simulation can be well predicted by our 3D SPH code. For this test case, Eq. (25) is used as the EOS for the simulation. The initial conditions on the left and right sides of the simulation domain are given by

$$\left(\rho\ (\mathrm{kgm}^{-3}),\, v\ (\mathrm{ms}^{-1}),\, p\ (\mathrm{Pa})\right) = \begin{cases} (1.0, -2.0, 0.4)\ , & \text{for } 0.0 < x < 0.5\ ; \\ (1.0, 2.0, 0.4)\ , & \text{for } 0.5 < x < 1.0\ . \end{cases} \tag{34}$$

The pressure and velocity distributions along the shock tube at a time of 0.15 s are shown in Figs. 2 and 3, respectively. A perusal of these figures indicates that our predictions using the SPH method are in excellent agreement with the analytical results [29].

3.2 1D cavitating flow in an open tube

The second test case proposed by Liu et al. [16] is used to validate the cavitation model implemented in our 3D SPH

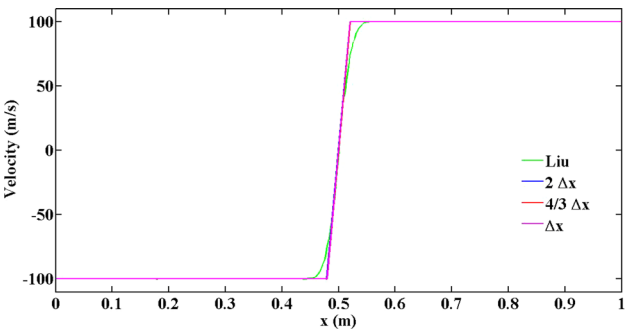

Fig. 5 Comparison of the SPH predictions of the velocity distribution along two water streams at a time of 0.2 ms for three different resolutions with those for a conventional mesh-based method of Liu et al. [16]

Table 1 Coefficients of the JWL model for the 1D PETN detonation

ρ_0 (kg/m^3)	A (Pa)	B (Pa)	R_1	R_2	w	E_0 (J/kg)
1765	6.17×10^{11}	1.6926×10^{10}	4.4	1.2	0.25	5.722×10^{6}

code. For this test case, Eq. (28) is used as the EOS for the simulation. The initial conditions on the left and right sides of the simulation domain for this water–water Riemann problem are prescribed as follows:

$$\left(\rho\ (\mathrm{kg/m^{-3}}),\ v\ (\mathrm{ms^{-1}}),\ p\ (\mathrm{Pa})\right) = \begin{cases} (1000, -100, 100, 000)\ , & 0.0 < x < 0.5\ ; \\ (1000, 100, 100, 000)\ , & 0.5 < x < 1.0\ . \end{cases} \tag{35}$$

The numerical predictions of the distributions of pressure and velocity along two water streams obtained using SPH for three different resolutions (Δx, $4/3\Delta x$, $2\Delta x$ with $\Delta x = 0.5$ mm) at a time of 0.2 ms is compared with a numerical result obtained using a conventional mesh-based method with a one-fluid cavitation model [16] in Figs. 4 and 5, respectively. It can be seen that the SPH predictions are generally in good conformance with the mesh-based predictions.

3.3 1D PETN detonation

The simulation of the 1D pentaerythritol tetranitrate (PETN) explosive detonation is conducted in order to validate the JWL model incorporated in our 3D SPH code. For this test case, Eq. (24) was used as the EOS for the simulation. The JWL parameters for the 1D PETN detonation are summarized in Table 1 [30]. The total length of the PETN slab is 0.1 m. In our SPH simulation, the initial particle spacing is 0.0002 m and the time step is 1.0×10^{-9} s. The pressure distributions along the PETN slab for four different numbers of particles (namely for 250, 500, 1000, 2000 particles) at various distances along the slab is shown in Fig. 6. An examination of this figure shows that the peak pressure predicted by the SPH simulations converges to the experimental peak pressure of 33.5 GPa.

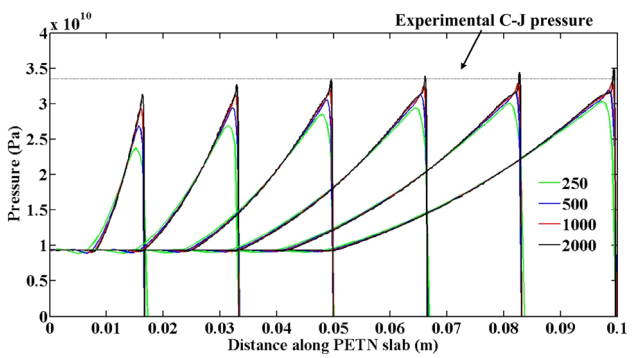

Fig. 6 SPH predictions of the pressure distribution along the 1D PETN slab during the detonation process for four different numbers of particles

3.4 3D high-velocity impact

The impact of a 3D aluminum (Al) sphere on a thin Al plate is simulated in order to validate the elastic–perfectly plastic constitutive model implemented in our 3D SPH code. The Mie–Gruneisen equation and Johnson–Cook parameters for Al–Al impact are summarized in Tables 2 and 3 [21], respectively. The radius of the Al sphere is 0.01 m, and the velocity of the sphere is 6180 m s^{-1}. The length, width and height of the Al plate are 0.1 m, 0.004 m and 0.1 m, respectively. A total of 690,243 particles were used in this simulation. The SPH predictions of the high-velocity impact at a time of 16 μs are shown in Fig. 7. Qualitatively, it is noted that the overall general shape of the debris cloud obtained from the simulation is similar to that obtained from some experimental data (cf. Fig. 8 [31] with Fig. 7). Furthermore, the impact model has also been validated quantitatively in our previous research paper [14] using the Armco iron cylinder impact test case study.

4 Simulation of a 3D underwater explosion within a cylinder

4.1 Underwater explosion within a rigid cylindrical structure

After validation of the various components of our general 3D SPH code, we will focus now on the simulation of a 3D underwater explosion in a rigid cylinder. The initial geometry of this problem is shown in Fig. 9, which is the same as the initial configuration in [17]. The diameter and the height of the cylinder are 0.0889 m and 0.2886 m, respectively. In order to enable a direct comparison of our predictions with those from [17], the explosion model used here will be simplified to a high-pressure gas bubble. The spherical explosive gas bubble has a diameter of 0.03 m and is located at the center of the

Table 2 Coefficients of the Mie–Gruneisen model for Al–Al high-velocity impact

ρ_0 (kg/m^3)	C (m/s)	S	G (MPa)	Y_0 (MPa)	Γ
2710	5300	1.5	2.76×10^{4}	550	1.70

Table 3 Johnson–Cook parameters for Al–Al high-velocity impact

A (MPa)	B (MPa)	C	n	k	T_{room} (K)	T_{melt} (K)	C_{v} (J/kg K)
175	380	0.0015	0.34	1.0	273	775	875

cylinder. The EOS for the gas bubble is described by Eq. (25). The initial pressure and density of the explosive gas bubble are set to values of $p_{\text{g}} = 2 \times 10^9$ Pa and $\rho_{\text{g}} = 1770$ kg m^{-3}, respectively. The parameter γ in Eq. (25) is set to a value of 2.0 for this simulation. Tait's equation [Eq. (28)] is used in the simulation. The initial pressure and density of the water in the cylinder are assumed to be $p_{\text{w}} = 1 \times 10^5$ Pa and $\rho_{\text{w}} = 1000$ kg m^{-3}, respectively. The modified Schmidt cavitation model is utilized when the pressure is smaller than the saturated vapor pressure. In the simulation, the latter assumes a value of 3165 Pa. The initial particle spacing is $\Delta x = 0.001$ m, and 1,800,000 particles are used for this simulation. Furthermore, three layers of dummy particles are included and used to impose the no-slip wall (solid) boundary conditions. The time step used for this simulation is $\Delta t = 1.0 \times 10^{-8}$ s. The simulation was conducted on a computational platform with Intel E5-2683 CPUs. The total computational time (or, wall clock time) for the simulation, consisting of 12,000 time steps, is 120 CPU hours.

Figure 10a1–a8 depicts the temporal evolution of the pressure distribution at the following times, namely at 15, 30, 45, 60, 75, 90, 105 and 120 μs. After the initiation of the explosion, a compressive shock wave is created. This shock wave propagates radially in all directions to the solid boundary of the rigid cylinder (cf. Fig. 10a1). Subsequently, the reflected shock wave from the solid wall (of the cylinder) interacts with the expanding high-pressure gas, and as a result, a rarefaction wave is generated (cf. Fig. 10a2). A cavitation zone

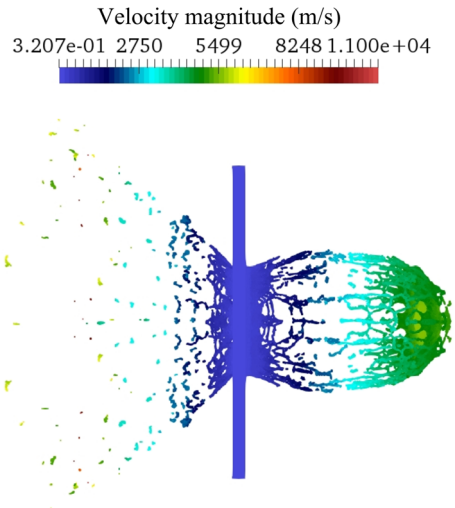

Fig. 7 SPH prediction of the debris cloud produced by the impact of an Al sphere on a thin Al plate

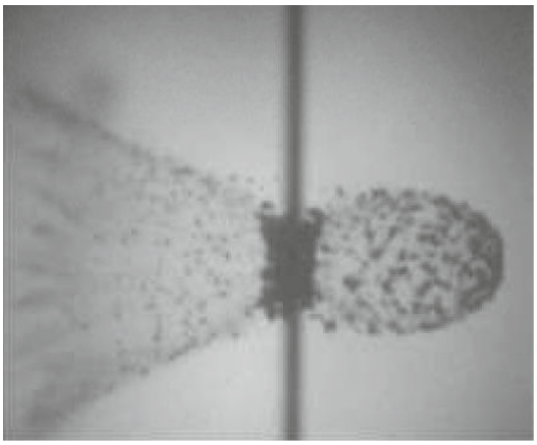

Fig. 8 Experimental measurement of the debris cloud produced by the impact of an Al sphere on a thin Al plate [31]

(white zone) may form near the bubble surface if the rarefaction wave is strong enough. Indeed, the rarefaction wave impacts the wall of the rigid cylinder and is reflected from this boundary, and induces a cavitation near the solid boundary (cf. Fig. 10a3–a5). At the end of this process, the cavitation zone collapses as a result of the compression generated by the compressive shock wave (Fig. 10a6–a8). The temporal evolution of the pressure distribution predicted using the SPH method (Fig. 10a1–a8) can be compared to that obtained using the Arbitrary Lagrangian–Eulerian (ALE) method [17] (see Fig. 10b1–b8). A careful perusal of these figures shows that the shock wave propagation and the location of the cavitation predicted by the SPH method are in good conformance with those predicted by the ALE method.

Figure 11 exhibits the SPH prediction of the pressure history at the center location of the side wall, obtained with

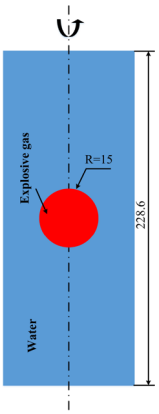

Fig. 9 Initial geometry of underwater explosion within a rigid cylinder. The dimensions shown in the diagram are in millimeter

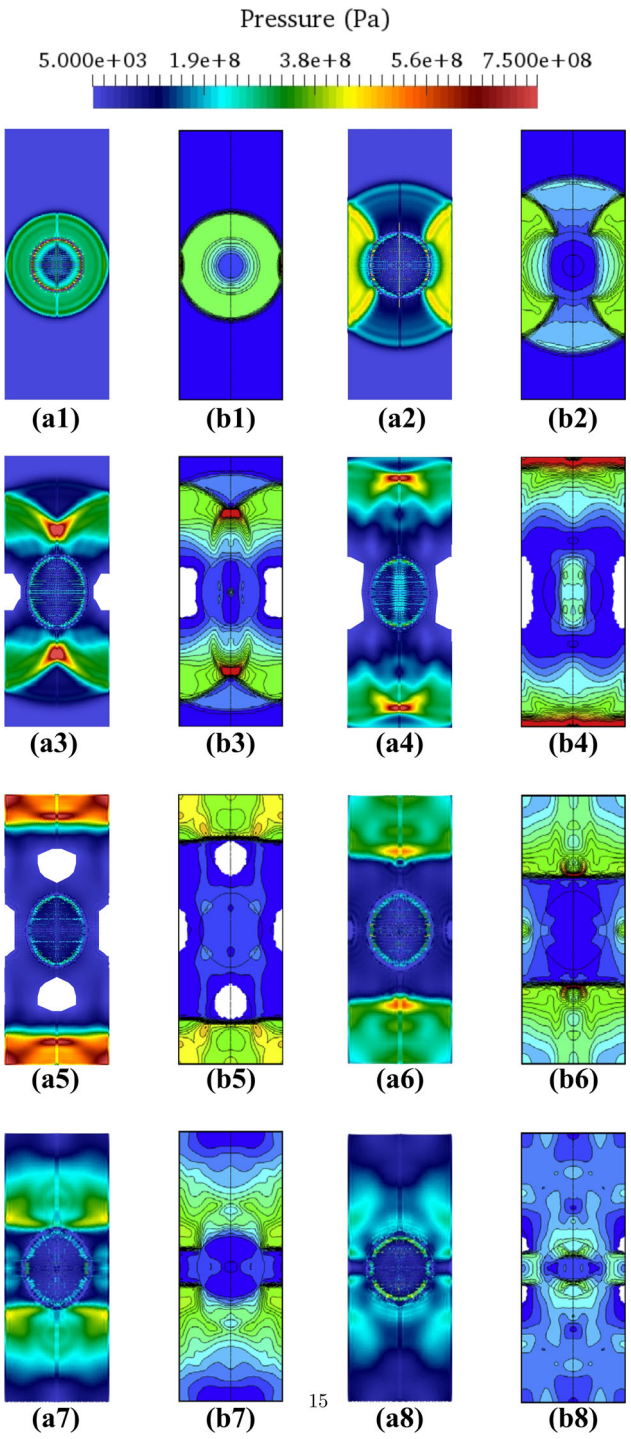

Fig. 10 Predictions of the pressure distribution of an underwater explosion within a rigid cylinder from 15–120 μs obtained using the SPH method (**a1**–**a8**) and the ALE method (**b1**–**b8**) [17]

initial particle spacings of Δx and $1.5\Delta x$ where $\Delta x = 0.001$ m. These results are compared to the numerical simulation conducted by Liu et al. [16] using a mesh-based approach. For an initial particle spacing of Δx, it is noted that the pressure at the midline wall predicted by the SPH method increases rapidly to a value of 0.660 GPa at a time

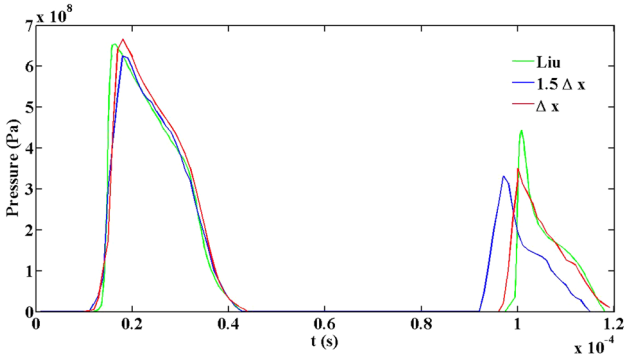

Fig. 11 Prediction of the pressure histories at the midline wall of a rigid cylinder obtained by SPH for two different particle resolutions compared with those obtained from Liu et al. [16]

of 19 μs. Subsequently, the pressure near the wall decreases and a cavitation region is induced at 42 μs. This cavitation region finally collapses completely at about 98 μs. An examination of Fig. 11 shows that the first increase and decrease in the pressure and the time at which cavitation occurs are in good agreement with the results of Liu et al. [16]. For the SPH prediction with an initial particle spacing of Δx, the pressure is seen to increase to a peak value again at a time of 102 μs, followed subsequently by the creation of a second cavitation region at about 117 μs. These SPH predictions for the time of occurrence of the second pressure peak and of the second cavitation region are earlier than those predicted by Liu et al. [16]. Furthermore, the SPH method predicts a value for the second pressure peak of 0.35 GPa which is about 18% smaller than that predicted by Liu et al. [16] (viz. the latter study predicts a value for the second pressure peak of 0.43 GPa).

The differences in the predictions given by SPH and ALE are reasonable (and perhaps to be expected). Firstly, we conducted a full (general) 3D underwater explosion within a rigid cylinder simulation, in contrast to previous investigations [16,17] which exploited the cylindrical symmetry in the problem to conduct 2D simulations using a cylindrical coordinate system. Secondly, it is seen that a better numerical pressure distribution (cf. Fig. 11) can be obtained from the SPH method by simply using a larger number of particles. However, increasing the number of particles in the simulation over and above what has been used in our current simulations is beyond the capability of our currently available computational resources. Thirdly, the artificial viscosity used in our SPH simulations tends to suppress the shock wave oscillation. In contrast, Liu et al. [16] used an integral–differential form to treat the relationship across the cavitation boundary. Furthermore, the SPH approach is a Lagrangian particle method in which the calculation of the physical quantities is based on the summation of the particles in a support domain (determined by the nature of the kernel function

used), in stark contrast to a mesh-based numerical method. Lastly, the implementation of the boundary conditions (utilizing dummy particles) in SPH is totally different from how boundary conditions are incorporated in conventional mesh-based methods. Given these differences, the comparison of numerical results provided by the SPH and ALE method is reasonable, and from this perspective, we conclude that the SPH methodology is able to adequately capture the details of shock wave propagation and cavitation phenomenology in underwater explosion simulations.

4.2 3D underwater explosion within a deformable aluminum tube

We consider the simulation of a 3D underwater explosion within an aluminum tube. The initial configuration for this simulation conforms exactly to the initial geometry used in the experiment conducted by Chambers et al. [30] (see Fig. 12).

The case considered herein involved placing an explosive charge within a deformable structure consisting of an Al tube with the following dimensions: The tube has a length of 19.2 cm, an outer diameter of 10.2 cm and a wall thickness of 0.7 cm. A small explosive charge consisting of 3.0 g PETN is suspended inside the Al tube which is filled with distilled water. The JWL parameters for the PETN detonation are summarized in Table 1. The Mie–Gruneisen and Johnson–Cook model parameters for Al that are used in our simulation are presented in Tables 2 and 3, respectively. Both the Mie–Gruneisen EOS and Tait's equation are utilized in our compressible fluid simulation. The Mie–Gruneisen

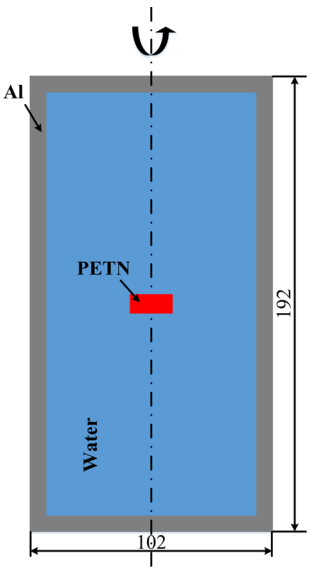

Fig. 12 Initial geometry of an underwater explosion in a deformable aluminum tube. The dimensions shown in the diagram are in millimeter

parameters for water used in the simulation are summarized in Table 4 [15]. The initial particle spacing used for the simulation is 0.001 m. Furthermore, a total of 870,000 particles were used in the simulation which was conducted with a time step is 1×10^{-8} s. The Open-MP programming interface has been used in order to improve the computational efficiency. The simulation was conducted on a computational platform with Intel E5-2683 CPUs. A total computational (wall clock) time of 78 CPU hours was required to complete the simulation which involved executing 12,000 time steps.

SPH predictions of the pressure and the velocity distributions of the underwater explosion using Tait's equation are exhibited in Figs. 13 and 14, respectively, at eight different times, namely at 15, 30, 45, 60, 75, 90, 105 and 120 μs. The results of our numerical simulations for this case seem to suggest that clearer (better delineated) pressure contours for the time interval from 75 to 120 μs can be obtained using Tait's equation in comparison with those obtained using the Mie–Gruneisen EOS. From a careful examination of Fig. 13, it is evident that the initiated shock wave propagates radially in all directions within the water medium inside the Al tube. This shock wave impacts the inside surface of the Al tube at about 18 μs. At this time, it is seen that the pressure at the midline wall increases rapidly and the surface of the Al tube is deformed owing to the force on the tube generated by the shock wave (see Fig. 13d–f). Furthermore, note that the degree of deformation at the midline wall is larger than that at other parts of the tube owing to the fact that the velocity at the midline wall is a maximum on the tube at this location (see Fig. 14). As the shock wave propagates, a cavitation zone is created at a time of about 30 μs near the centerline wall as the rarefaction wave hits the Al tube. Subsequently, this cavitation zone collapses at a time of about 48 μs, as the pressure in the cavitation zone increases as a result of the compressive shock wave. This is evident in Fig. 15) and demonstrates clearly that the generation and collapse of a cavitation zone can be predicted by the SPH simulation.

Figure 15 also exhibits a comparison between the pressure distribution predicted by our SPH simulation with some experimental data [32]. Note that the predicted peak pressures obtained using SPH with the Mie–Gruneisen EOS and Tait equation are about 0.585 GPa and 0.560 GPa, respectively. These values for the peak pressure compare well with the experimental value of 0.620 GPa. Furthermore, it is seen that the peak pressure obtained using the Mie–Gruneisen EOS is in better conformance with the experimental value

Table 4 Coefficients of the Mie–Gruneisen model for water

ρ_0 (kg/m^3)	C_0 (km/s)	S_1	S_2	S_3	γ	α	E_0 (J)
1000	1480	2.56	1.986	1.2286	0.5	0	0

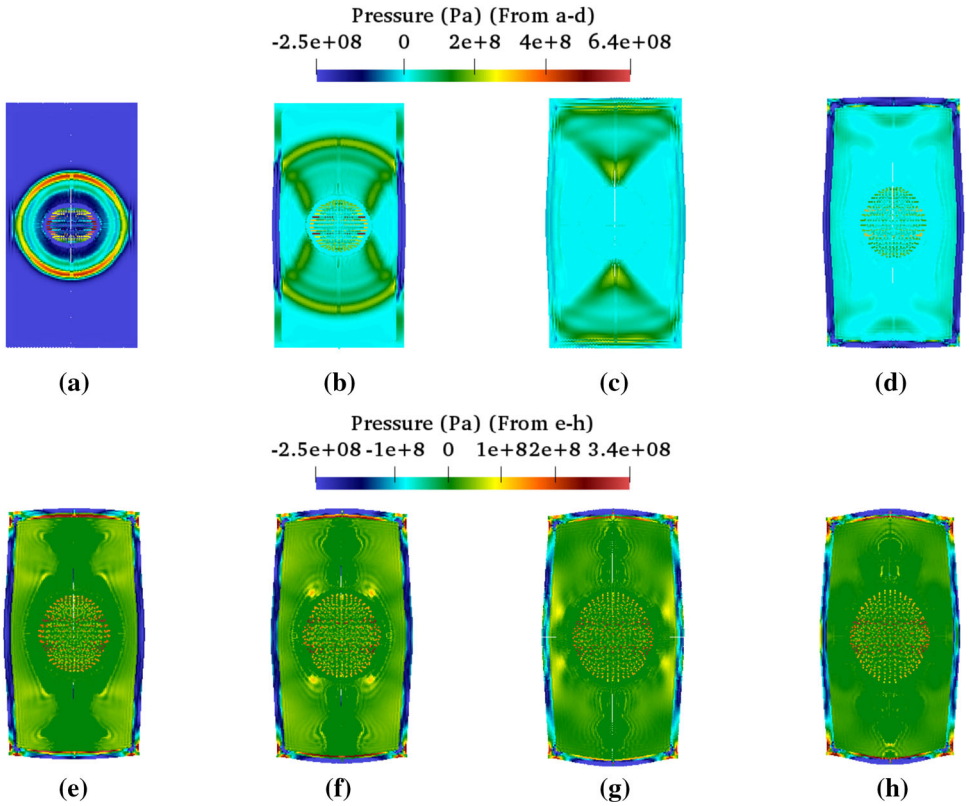

Fig. 13 Predictions of the pressure distribution of an underwater explosion in an aluminum tube obtained using SPH for a time interval from 15 to 120 μs

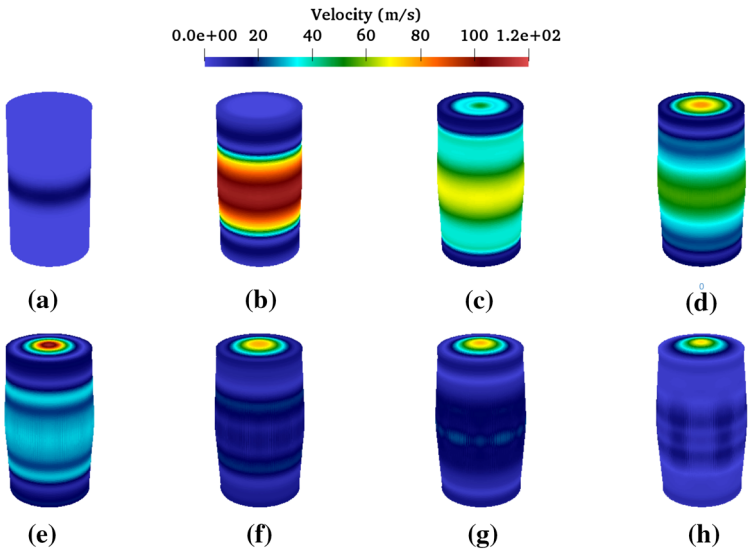

Fig. 14 Predictions of the velocity distribution of an underwater explosion in an aluminum tube obtained using SPH for a time interval from 15 to 120 μs

than that obtained using the Tait equation. Moreover, the generation and collapse of the cavitation zones are similar to the experimental results. The displacements at the midline wall have also been compared with the experimental results, and it is found that the relative errors between the predicted and experimental results are generally less than about 20% (cf. Table 5).

The discrepancy between the predicted pressure and displacements and the associated experimental measurements can be attributed to a number of factors. Firstly, only two EOS models (namely Tait's equation and the Mie–Gruneisen EOS) have been used to model the liquid compression in our simulations. There are a number of alternative EOS compressible fluid models that will need to be considered and evaluated to

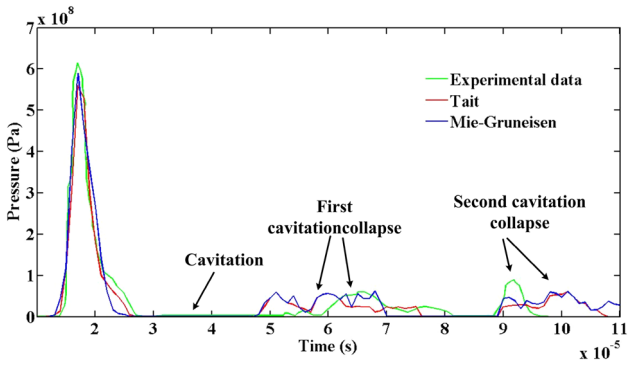

Fig. 15 Prediction of the pressure histories at the midline wall of a deformable cylinder obtained by SPH compared with some experimental data [32]

determine whether these models can give predictions that are in better conformance with the experimental measurements (viz. better than what has been obtained in the current study). Secondly, although less likely, the discrepancy between the predictions and the experimental measurements may reside in the form of the kernel function used in the determination of the physical quantities in SPH. Certainly, a number of different kernel functions will need to be considered (in future efforts) and evaluated in terms of their effects on the SPH predictions of the pressure and displacement. Thirdly, we have used only the Mie–Gruneisen model for the simulation of the impact on the Al tube. Certainly, a number of additional solid impact models (e.g., Cowper–Symonds model [33]) will need to be tested and evaluated in terms of their effects on the prediction of the pressure and displacement for underwater explosion problems. In view of this, it is stressed that given the expected model and experimental errors, current predictions obtained with our SPH method for the structural deformation resulting from an underwater explosion seem reasonable. In the future, it is expected that these predictions can be further improved with the incorporation of more sophisticated models for liquid compression and for solid impact.

5 Conclusion

In this paper, the SPH method in conjunction with a modified Schmidt model has been used to simulate a fully 3D underwater explosion in a both rigid and deformable (Al) tube. The proposed methodology has been implemented as part of a general 3D in-house SPH code that incorporates the Open-MP parallel programming interface to provide the computational efficiency required to conduct simulations with large numbers of particles. Various components of SPH code have been validated using a number of test cases, namely the Sjögreen test case, a 1D cavitating flow in an open tube test case, a 1D PETN detonation test case and a 3D high-velocity impact test case. After this comprehensive validation, the SPH code has been applied to the simulation of a fully 3D underwater explosion in a rigid cylinder and in a deformable aluminum tube. These 3D SPH predictions of an underwater explosion have been compared with other numerical simulations of the problem using alternative approaches, as well as with some available experimental data.

The conclusions of this study can be summarized as follows. The cavitation phenomenon in an underwater explosion in a cylinder (rigid or deformable) is well predicted generally using the SPH method in conjunction with the modified Schmidt cavitating model. Predictions of the pressure distribution and the deformation of the structure obtained from the SPH method are generally in reasonable to good conformance with experimental measurements as well as with other numerical simulations. To the best of our knowledge, this appears to be first time that a fully explicit 3D underwater explosion in either a rigid or a deformable cylinder incorporating properly the cavitation phenomenology has been successfully simulated using the SPH method.

With respect to future work, the solid impact Cowper–Symonds model, the Mie–Gruneisen compressible fluid model and the one-fluid cavitating model will be implemented and incorporated into our SPH code. The damage to various structures arising from an underwater explosion will be conducted using these models and validated using available experimental data in order the assess the capability of the modeling scheme to predict structural damage.

Table 5 Comparison of the simulation and experimental displacements (mm) at midline wall, where %error = |simul. − expt.|/expt. × 100

Time (ms)	0.01	0.02	0.03	0.04	0.06	0.08	0.1	0.15
Expt. (experiment)	0.0	0.50	1.20	2.00	3.33	4.17	4.65	5.50
Simul. (Tait)	0.0	0.41	1.00	1.61	2.93	3.85	4.10	5.10
Simul. (Mie–Gruneisen)	0.0	0.42	1.00	1.70	2.95	3.86	4.12	5.20
%Error (Tait)	0.0	18.0	16.6	19.5	12.0	7.67	11.8	7.27
%Error (Mie–Gruneisen)	0.0	16.0	16.6	15.0	11.4	7.43	11.3	5.40

Acknowledgements The authors acknowledge the facilities of the Shared Hierarchical Academic Research Computing Network (SHARCNET: www.sharcnet.ca) and Compute/Calcul Canada. The first author is supported by the China Scholarship Council (No. 201506030072) and the Natural Sciences and Engineering Research Council of Canada (NSERC).

Compliance with ethical standards

Conflict of interest On behalf of all authors, the corresponding author states that there is no conflict of interest.

References

1. Shin YS (2004) Ship shock modeling and simulation for far-field underwater explosion. Comput Struct 82(23–26):2211–2219
2. Kim J, Shin H (2008) Application of the ALE technique for underwater explosion analysis of a submarine liquefied oxygen tank. Ocean Eng 35(8–9):812–822
3. Wang Y, Liao C, Wang J, Wang W (2018) Numerical study for dynamic response of marine sediments subjected to underwater explosion. Ocean Eng 156:72–81
4. Zhang Z, Wang C, Wang L, Zhang A, Silberschmidt VV (2018) Underwater explosion of cylindrical charge near plates: analysis of pressure characteristics and cavitation effects. Int J Impact Eng 121:91–105
5. Gingold RA, Monaghan JJ (1977) Smoothed particle hydrodynamics: theory and application to non-spherical stars. Mon Not R Astron Soc 181(3):375–389
6. Lucy LB (1977) A numerical approach to the testing of the fission hypothesis. Astron J 82:1013–1024
7. Swegle J, Attaway S (1995) On the feasibility of using smoothed particle hydrodynamics for underwater explosion calculations. Comput Mech 17(3):151–168
8. Liu M, Liu G, Lam K (2002) Investigations into water mitigation using a meshless particle method. Shock Waves 12(3):181–195
9. Fan H, Li S (2017) Parallel peridynamics-SPH simulation of explosion induced soil fragmentation by using OpenMP. Comput Part Mech 4(2):199–211
10. Fan HF, Li SF (2017) A peridynamics-SPH modeling and simulation of blast fragmentation of soil under buried explosive loads. Comput Methods Appl Mech Eng 318:349–381
11. Zhao XH, Wang GH, Lu WB, Yan P, Chen M, Zhou CB (2018) Damage features of RC slabs subjected to air and underwater contact explosions. Ocean Eng 147:531–545
12. Zhang A, Yang W, Huang C, Ming F (2013) Numerical simulation of column charge underwater explosion based on SPH and BEM combination. Comput Fluids 71:169–178
13. Chen JY, Lien FS (2018) Simulations for soil explosion and its effects on structures using SPH method. Int J Impact Eng 112:41–51
14. Chen JY, Peng C, Lien FS (2019) Simulations for three-dimensional landmine detonation using the SPH method. Int J Impact Eng 126:40–49
15. Liu GR, Liu MB (2003) Smoothed particle hydrodynamics: a meshfree particle method. World Scientific, Singapore
16. Liu T, Khoo B, Xie W (2004) Isentropic one-fluid modelling of unsteady cavitating flow. J Comput Phys 201(1):80–108
17. Jafarian A, Pishevar A (2017) An exact multiphase Riemann solver for compressible cavitating flows. Int J Multiph Flow 88:152–166
18. Monaghan JJ (1988) An introduction to SPH. Comput Phys Commun 48(1):89–96
19. Randles PW, Libersky LD (1996) Smoothed particle hydrodynamics: some recent improvements and applications. Comput Methods Appl Mech Eng 139(1–4):375–408
20. Johnson GR, Cook WH (1983) A constitutive model and data for metals subjected to large strains, high strain rates and high temperatures. In: Proceedings of the 7th international symposium on ballistics, vol 21, The Hague, The Netherlands, pp 541–547
21. Libersky LD, Petschek AG, Carney TC, Hipp JR, Allahdadi FA (1993) High strain Lagrangian hydrodynamics: a three-dimensional SPH code for dynamic material response. J Comput Phys 109(1):67–75
22. Lee EL, Tarver CM (1980) Phenomenological model of shock initiation in heterogeneous explosives. Phys Fluids 23(12):2362–2372
23. Steinberg D (1987) Spherical explosions and the equation of state of water. Technical report, Lawrence Livermore National Laboratory, CA (USA)
24. Wang P, Zhang A, Ming F, Sun P, Cheng H (2019) A novel non-reflecting boundary condition for fluid dynamics solved by smoothed particle hydrodynamics. J Fluid Mech 860:81–114
25. Xie W, Liu T, Khoo B (2006) Application of a one-fluid model for large scale homogeneous unsteady cavitation: the modified Schmidt model. Comput Fluids 35(10):1177–1192
26. Monaghan JJ (1994) Simulating free surface flows with SPH. J Comput Phys 110(2):399–406
27. Adami S, Hu XY, Adams NA (2012) A generalized wall boundary condition for smoothed particle hydrodynamics. J Comput Phys 231(21):7057–7075
28. Peng C, Wu W, Yu HS, Wang C (2015) A SPH approach for large deformation analysis with hypoplastic constitutive model. Acta Geotech 10(6):703–717
29. Sirotkin FV, Yoh JJ (2013) A smoothed particle hydrodynamics method with approximate Riemann solvers for simulation of strong explosions. Comput Fluids 88:418–429
30. Chambers G, Sandusky H, Zerilli F, Rye K, Tussing R, Forbes J (2001) Pressure measurements on a deforming surface in response to an underwater explosion in a water-filled aluminum tube. Shock Vib 8(1):1–7
31. Plassard F, Mespoulet J, Hereil P (2011) Hypervelocity impact of aluminium sphere against aluminium plate: experiment and LS-DYNA correlation. In: Proceedings of the 8th European LS-DYNA users conference, Strasbourg, France, pp 23–24
32. Wardlaw JA, McKeown R, Luton A (1998) Coupled hydrocode prediction of underwater explosion damage. Technical report, Naval Surface Warfare Center, Indian Head, MD
33. Cowper GR, Symonds PS (1957) Strain-hardening and strain-rate effects in the impact loading of cantilever beams. Technical report, Brown University, Providence, RI